

Research paper

# Toward extreme high-temperature supercritical CO<sub>2</sub> power cycles: Leakage characterization of ceramic 3D-printed heat exchangers

Rasoul Bayaniahangar<sup>a</sup>, Ikehukwu Okoh<sup>a</sup>, Kashif Nawaz<sup>b</sup>, Joseph Cesarano<sup>c</sup>, Sajjad Bigham<sup>a,\*</sup>

<sup>a</sup> Department of Mechanical Engineering-Engineering Mechanics, Michigan Technological University, Houghton, MI, USA

<sup>b</sup> Oak Ridge National Laboratory, Oak Ridge, TN, USA

<sup>c</sup> Robocasting Enterprises, Albuquerque, NM, USA

## ARTICLE INFO

## Keywords:

Ceramics  
3D-printing  
Leakage characterization  
Heat exchanger  
Permeability

## ABSTRACT

Future supercritical carbon dioxide (sCO<sub>2</sub>) Brayton power cycles demand high-performance gas-to-gas heat exchangers (HXs) operating under extreme temperature and pressure conditions at which most existing superalloy materials fail to function safely. Ceramic HXs are deemed excellent candidates for advanced sCO<sub>2</sub> power plants as they can withstand high-temperature working environments. Particularly, ceramic 3D printing enables compact HX topologies employing complex and efficient heat transfer features. However, ceramic 3D-printed walls separating hot and cold flow streams are susceptible to a through-plane leakage inherent to a powder-based manufacturing process, including ceramic 3D printing. A potential leakage through ceramic separating walls poses a significant challenge in developing reliable ceramic 3D-printed HXs and could deteriorate thermal performance. In this study, various parameters, including feedstock slurry, 3D-printing direction, and post-processing conditions, are considered, for the first time, to characterize the argon gas leakage rate associated with alumina 3D-printed parts. Three 3D-printed ceramic structures of flat plates, curved tubes, and small-scale plate-and-frame HXs with various thicknesses are systematically studied to determine powder and ceramic 3D-printing conditions to eliminate the through-plane leakage. The results showed that an alumina 3D-printed plate with a thickness of 0.75 mm demonstrates a permeability of  $6 \times 10^{-4}$  milli-darcy. An alumina 3D-printed tube with a wall thickness of 0.9 mm revealed a permeability of  $9.6 \times 10^{-7}$  milli-darcy. Furthermore, leakage test results of functional 3D-printed modules showed a dependency on the 3D-printing direction. Particularly, alumina cell-scale HXs employing 1.5-mm-thick horizontal and vertical 3D-printed separating walls demonstrated impermeability and gas permeability of  $7.2 \times 10^{-5}$  millidarcy, respectively. Insights gained from the present study facilitate the development of complex ceramic 3D-printed HXs and other balance of plant components for next-generation high-temperature high-pressure sCO<sub>2</sub> power cycles.

## 1. Introduction

Supercritical carbon dioxide (sCO<sub>2</sub>) closed Brayton cycles are widely considered as one of the most promising candidates for next-generation high-efficiency power plants. The sCO<sub>2</sub> power cycles demand high-performance heat exchangers (HXs) functioning under extreme simultaneous temperature and pressure conditions [1,2]. Metals and superalloys including high-grade steels and nickel-based alloys are current choices of materials for high-temperature heat exchanger applications. Metal and superalloy materials, however, experience severe degradation at elevated temperatures and lose their thermo-mechanical properties

and strength at temperatures exceeding 800 °C [3].

If designed properly and manufactured economically, ceramic heat exchangers could provide a promising recuperating solution for several emerging high-temperature applications such as sCO<sub>2</sub> power cycles, aero-engine recuperators, and industrial waste heat recovery. Ceramics offer many attractive features, including excellent mechanical strength at elevated temperatures combined with superior oxidation and creep resistances suitable for high-temperature, high-pressure gas-to-gas heat exchangers operating under highly oxidizing environments. Existing ceramic-based HX technologies are, however, primarily based upon conventional manufacturing approaches and thus bound to their

\* Corresponding author.

E-mail address: [sbigham@mtu.edu](mailto:sbigham@mtu.edu) (S. Bigham).

<https://doi.org/10.1016/j.addma.2022.102783>

Received 19 July 2021; Received in revised form 24 December 2021; Accepted 21 March 2022

Available online 24 March 2022

2214-8604/© 2022 Elsevier B.V. All rights reserved.

inherent limitations, including difficulty in machining and design flexibility [4–7]. Additive manufacturing (AM) of ceramics eliminates constraints faced by traditional fabrication approaches and thus enables the manufacturing of complex features with enhanced thermo-mechanical characteristics for next-generation high-temperature high-pressure heat exchangers [8–11]. In the use of ceramic 3D-printed materials for thermo-fluidic energy applications, understanding the permeability of walls enclosing a working fluid is of paramount importance. A through-plane leakage between cold and hot flow streams could degrade the heat recovery potential of ceramic 3D-printed thermo-fluidic devices, including heat exchangers.

The permeability of ceramic modules depends on the quality of feedstock slurry and fabrication process as well as subsequent post-processing steps such as drying and sintering. A review on ceramic foams showed that permeability drastically varies from  $1.2 \times 10^{-7}$  to  $1.0 \times 10^{-11} \text{ m}^2$  within a small porosity range of 0.75 – 0.95 [12]. Lipowiecki et al. [13] made a comparison between two rapid-prototyped (i.e., 3D printing and micro-stereo-lithography) artificial bone scaffold structures. The permeability of the porous structures was evaluated using both water and glycerol-water as working fluids, which resulted in permeability values ranging from  $1.84 \times 10^{-10}$  to  $4.19 \times 10^{-9} \text{ m}^2$ , with porosities ranging from 30% to 70%. Dey et al. [14] performed permeability assessments of cordierite bonded porous SiC ceramics. With porosities ranging from 30.1% to 71.7%, the resulting Darcian permeability coefficient ranged from  $10^{-13}$  to  $10^{-10} \text{ m}^2$ . Gómez-Martín et al. [15] performed permeability and mechanical integrity experiments on porous biomorphic SiC ceramics employed as hot-gas filters. The porosity fractions of different samples was 45–72%, with Darcian permeability ranging from  $10^{-13}$  to  $10^{-12} \text{ m}^2$ , which falls within the range of granular filters reported by other studies. Biasetto et al. [16] explored the permeability of SiOC microcellular ceramic foams. With cell sizes ranging from 10 to 150  $\mu\text{m}$ , Darcian permeability values varied from  $10^{-13}$  to  $10^{-10} \text{ m}^2$  were obtained. Their results indicated that an increase in cell window size gives an increase in permeability. Moreira et al. [17] explored the permeability of ceramic foams (SiC – Al<sub>2</sub>O<sub>3</sub> mixture) with compressible and incompressible flows, which produced a Darcian permeability range of  $10^{-9}$  to  $10^{-6} \text{ m}^2$ . They then proposed an Ergun-type empirical correlation to predict permeability. However, most prior studies as listed above have focused on permeability assessment of porous ceramic foams, in contrast to highly dense structures of separating walls employed in ceramic 3D-printed heat exchangers.

There are limited studies examining permeability and controlling the leakage rate of functional ceramic thermo-fluidic devices. Mostly, the chemical vapor deposition (CVD) technique has been utilized to coat a barrier layer on ceramic structures and thus seal the device [18–21]. Since ceramic structures are produced through conventional fabrication approaches in separate parts and then assembled as a whole structure, the possibility of leakage at ceramic joints is a concern. Schmitt et al. [18] characterized permeability of CVD-coated structures and demonstrated two orders of magnitude reduction in permeability compared with non-coated structures. Bouquet et al. [22] characterized permeability of composite matrix of SiC and reported a reduction in permeability value with an increase in temperature. They suggested a lower thermal expansion coefficient of carbon fibers than SiC is the governing mechanism for this behavior, which accounts for a crack size reduction and subsequently a drop in leakage rate. Hayasaka et al. [23] introduced a new SiC/SiC production process termed Nano-Infiltration and Transient Eutectoid (NITE) to reduce gas permeability of ceramic assemblies. The helium gas leakage of NITE SiC/SiC tubes showed more than two orders of magnitude improvement compared with conventionally fabricated ceramic samples. However, the above permeability studies were mainly based upon ceramic products manufactured through conventional fabrication approaches.

In order to fill the gap as noted above, the present study aims to characterize gas leakage rates of ceramic 3D-printed modules for the first time to the best of the authors' knowledge. Here, the effects of

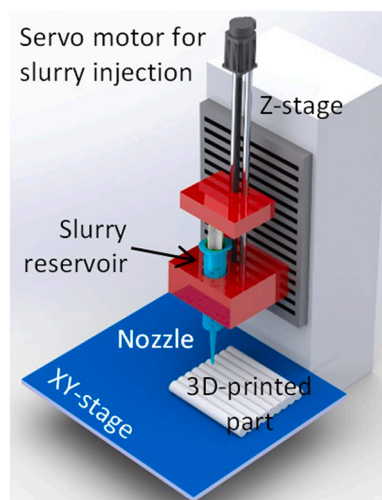


Fig. 1. A schematic of ceramic robocasting 3D printer.

several parameters, including feedstock slurry, 3D-printing direction, and post-processing conditions on leakage rate of alumina 3D-printed parts, are considered. The ceramic 3D-printed modules examined include flat plates, tubes, and small-scale plate-and-frame HXs. In the following, first, preparation of alumina feedstock slurry and 3D printing (i.e., robocasting) process are discussed. Next, the test facility for leakage characterization of ceramic 3D-printed structures is presented. Finally, leakage test results of alumina 3D-printed flat plates, curved tubes, and cell-scale HXs with horizontal and vertical separating walls are examined.

## 2. Methods

### 2.1. Preparation of alumina slurry

Two alumina compositions were considered. The first composition uses a fairly high-purity alumina powder of 99.8% and an average particle size of 1.9  $\mu\text{m}$  (i.e., feedstock A). The second alumina composition includes a high-purity alumina powder of 99.99% with an average particle size of  $\sim 0.5 \mu\text{m}$  (i.e., feedstock B). First, an aqueous alumina solution was prepared by adding the alumina powder to deionized water and ammonium polyacrylate with a molecular weight of 3500 g/mol as the dispersing agent. The alumina aqueous slurry was then mixed in a planetary ball mill for 6 h. Next, polyvinylpyrrolidone (i.e., PVP) with a molecular weight of 55000 g/mol and deionized water were mixed for 12 h. Finally, the aqueous alumina and binder solutions were mixed for another 1 h and used as the feedstock slurry for ceramic 3D printing.

### 2.2. Robocasting of alumina parts

The ceramic parts were 3D-printed through robocasting as an extrusion-based 3D-printing technique. The robocasting technology largely relies on the knowledge and fundamental understanding of the material properties necessary to develop an extrudable feedstock suitable for the robocasting 3D-printing process. Particle size distribution, surface area, morphology, and surface chemistry of the starting powders are very important. In addition to the characteristics of the starting powder, the carrier solvent and additives such as dispersants, binders, and plasticizers all affect the rheology and performance of the extrudable feedstock (i.e., paste). These properties also affect the drying and curing behaviors of the 3D-printed components and thus ultimately control the sintering behavior and final properties of the 3D-printed parts.

In the robocasting technique, the feedstock slurry is deposited in a layer-by-layer fashion. The feedstock slurry is loaded in a syringe

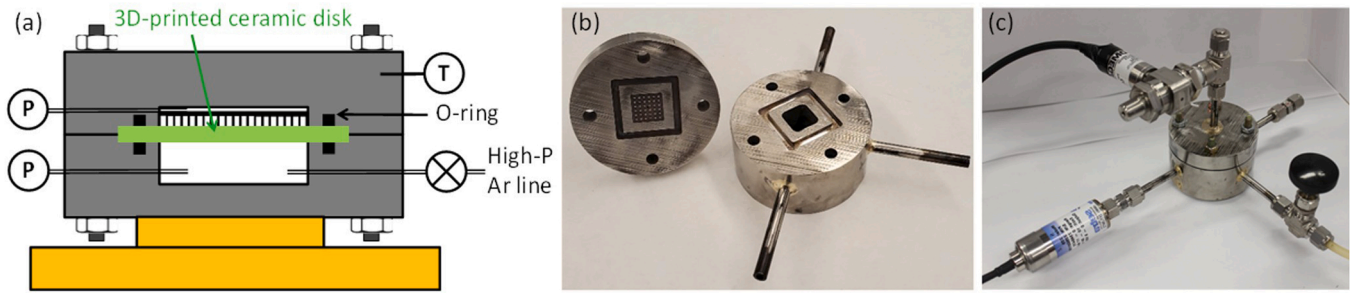


Fig. 2. (a) A schematic of the permeability test apparatus, (b) upper and lower chambers of the test setup, and (c) an image of the complete permeability test setup with two pressure sensors integrated.

extruder of a custom-made 3D printer with three degrees of freedom in the x, y, and z directions (cf. Fig. 1). The feedstock slurry is then extruded through a syringe needle as the stage moves in a predefined path. For a proper extrusion, the ceramic paste should exhibit specific rheological properties. The primary ones are good, consistent flow at a reasonable applied pressure, and appropriate yield stress upon extrusion. Here, the rheology of the feedstock slurry is optimized to demonstrate a shear-thinning behavior, thereby allowing extrusion of the ceramic slurry at a designed applied pressure. Once the ceramic slurry is deposited on the build plate, the 3D-printed green structures retain their shape due to the shear thinning behavior. The green body structure is then sintered at high temperatures (i.e., 1650 °C) to achieve high-density parts.

### 3. Test facility for leakage characterization of ceramic 3D-printed structures

#### 3.1. Characterization of ceramic 3D-printed plates

The leakage characterization of ceramic 3D-printed plates was conducted in a custom-made test setup shown in Fig. 2 at room temperature. The test apparatus consists of two stainless steel upper and lower plates with a 3D-printed ceramic plate sandwiched between the two plates (cf. Fig. 2a). A  $1.5 \times 1.5 \times 2.5 \text{ cm}^3$  cuboid chamber is carved into the lower plate with brazed tubes, as shown in Fig. 2b and c. The brazed tubes allow to (i) pressurize the lower stainless steel chamber with the argon gas to a target pressure level and (ii) integrate a pressure sensor for real-time pressure monitoring. As shown in Fig. 2b, the upper stainless steel plate is textured to resemble typical structures of a high-temperature, high-pressure (HTHP) heat exchanger (HX) design. With the lower chamber pressurized, the upper structures prevent large deformations of the 3D-printed ceramic plates.

Darcy's law formulates the flow of a fluid through a porous medium (Eq. (1)). This formula defines the permeability parameter,  $\kappa$ , as the resistance of the material to pass the flow through.

$$\kappa = \frac{\dot{m} \times \mu \times l}{\rho \times A \times \Delta P} \quad (1)$$

where  $\mu$  is argon dynamic viscosity, 0.000022 Pa.s,  $l$  is the plate

thickness,  $\rho$  is argon density,  $A$  is the surface area of the plate,  $2.25 \text{ cm}^2$ , and  $\Delta P$  is the pressure difference between the two sides of the 3D-printed ceramic plate. The ideal gas formula was used (Eq. (2)) to calculate the mass flow rate of the argon gas displaced through a ceramic 3D-printed plate. Knowing the pressure variation of the lower chamber during a test, time of testing, and temperature, the mass flow rate can be estimated by:

$$\dot{m} = \frac{V_{\text{lower chamber}} \times (P_{\text{initial}} - P_{\text{final}})}{\text{time} \times R_{s,\text{argon}} \times T} \quad (2)$$

#### 3.2. Characterization of ceramic 3D-printed tubes

The leakage rate of ceramic 3D-printed tubes was characterized through a similar approach discussed in the previous section at room temperature. Three ceramic 3D-printed tubes with various dimensions were studied. The ceramic tubes were initially pressurized with argon gas. The in-tube pressure variations were monitored as a function of time for 12 h to estimate the permeability of the ceramic tube structures. The intrinsic leakage rate of the test system and associated connections was established against an impermeable metal tube. Additionally, an alumina 3D-printed tube that was proved to be leak-free at room temperature was leak tested at combined high temperatures and pressures of 300 °C / 0.7 MPa, 350 °C / 1 MPa, and 400 °C / 1.4 MPa.

#### 3.3. Characterization of ceramic 3D-printed heat exchangers

In the next stage, the leakage rate of more functional ceramic energy devices in the form of 3D-printed heat exchangers was characterized at room temperature. The 3D-printed heat exchangers included hot and cold flow streams separated by thin ceramic 3D-printed walls. Two types of ceramic heat exchangers were studied to consider the effect of 3D-printing build orientation on the leakage rate. In the first type, the ceramic walls separating the hot and cold flow streams were 3D-printed in the horizontal direction (i.e., parallel to the build plate or XY-plane in Fig. 1). In the second type, the separating walls were 3D-printed in the vertical direction (i.e., vertical to the build plate or XZ-plane in Fig. 1). To study the leakage rate of the 3D-printed heat exchangers, a pressure potential between the hot and cold sides was established. The gas

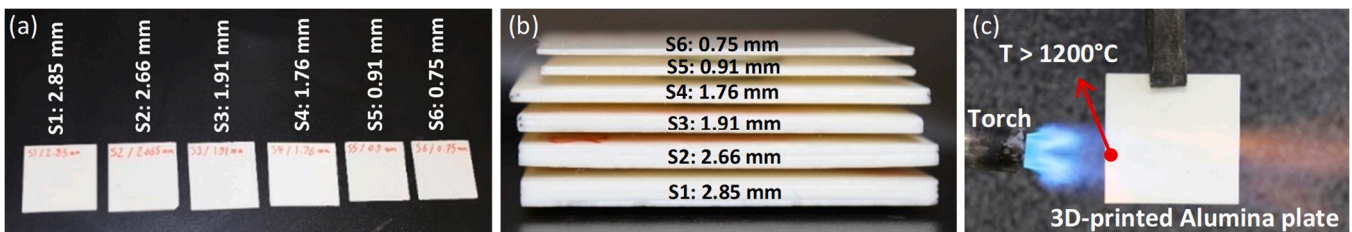


Fig. 3. (a) Images of the six 3D-printed alumina permeability test plates, (b) cross-sectional views of the test plates, and (c) 3D-printed test plates under a high-temperature torch flame.

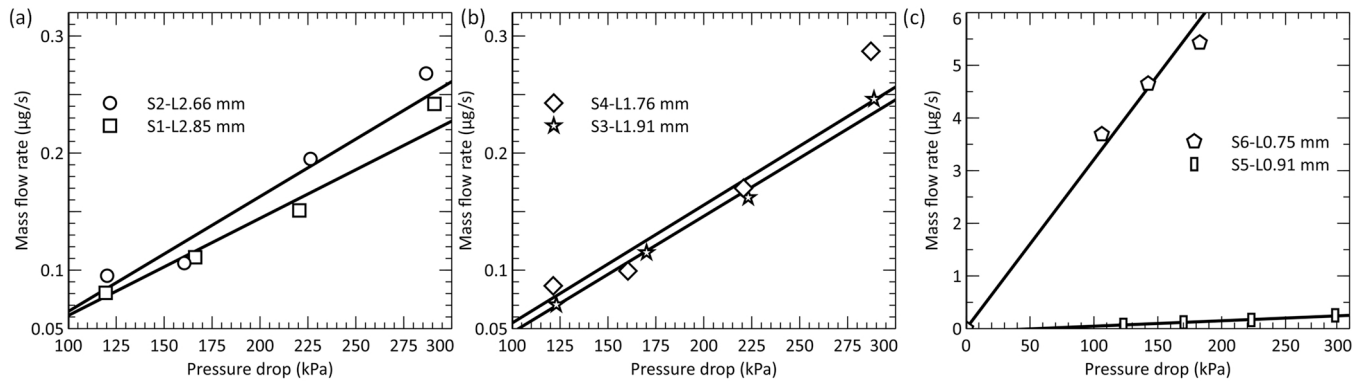


Fig. 4. Mass flow rate of the argon gas passed through samples (a) S1 and S2, (b) S3 and S4, and (c) S5 and S6 at different pressure drops (i.e., potentials) across the plates.

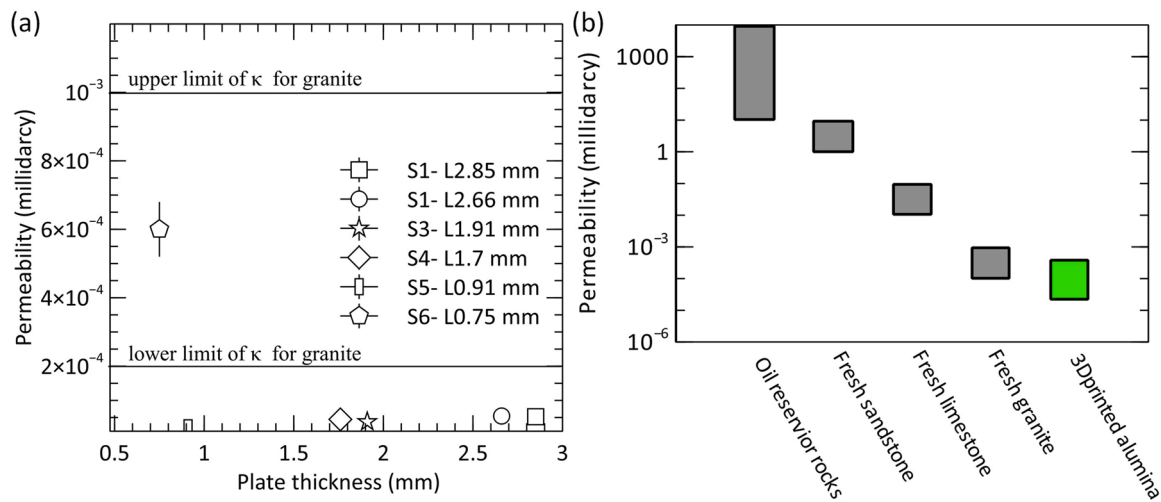


Fig. 5. (a) Permeability values of samples S1 to S6 at different plate thicknesses, and (b) a comparison of the permeability of the alumina 3D-printed plates against that of typical minerals.

leakage rate between the two sides determine the permeability of ceramic 3D-printed walls of heat exchanger modules.

## 4. Results and discussions

### 4.1. Ceramic 3D-printed flat plates

Fig. 3 shows six 3D-printed plate samples made of alumina feedstock A. The thicknesses of examined alumina plates are 2.85 (i.e., sample S1), 2.66 (i.e., sample S2), 1.91 (i.e., sample S3), 1.76 (i.e., sample S4), 0.91 (i.e., sample S5), and 0.75 mm (i.e., sample S6). These ceramic plates were sintered at a temperature of 1625 °C where they achieved an average density of 95–96% of theoretical density with an approximately 0.5% open porosity. To obtain a general sense of the high-temperature durability of these alumina 3D-printed plates, Fig. 3c depicts sample S1 under a high-temperature torch flame where the local temperature exceeds 1200 °C.

Fig. 4a to c show the mass flow rate of the argon gas leaked through the alumina 3D-printed plates at different pressure drops (i.e., potentials) across the plates. As shown, the variations of the mass flow rate are almost linear, with a change in the pressure drop consistent with the Darcy's formula. The curve slopes for samples S1 to S5 are close and approximately equal to  $10^{-15}$  kg/Pa-s, while the slope is one order of magnitude higher for sample S6 with a value of  $2 \times 10^{-14}$  kg/Pa-s. This clearly indicates that the permeability of the thinnest ceramic 3D-printed plate (i.e., sample S6) is higher.

Fig. 5a shows the permeability of samples S1 to S6 at different plate thicknesses. Fig. 5b compares the permeability of the alumina 3D-printed plates against that of typical minerals indicating a high quality of the alumina 3D-printed plates. As evident, samples S1 to S5 having a thickness range of 2.85–0.91 mm demonstrated a permeability value of  $0.5 \times 10^{-4}$  milli-darcy below the lower permeability limit of granite. Sample S6 with a thickness of 0.75 mm showed a permeability of  $6 \times 10^{-4}$  milli-darcy which is between the lower and upper permeability limits of granite. An uncertainty analysis indicated a maximum uncertainty of  $\pm 14\%$  associated with the reported permeability values.

Further investigation of the alumina 3D-printed composition employed suggested that the density of the sintered alumina plates for leakage tests was about 95–96% of theoretical density with an approximately 0.5% open porosity. Alumina feedstock A was composed of an alumina powder with a purity of 99.8% and an average particle size of 1.9  $\mu\text{m}$ . Next, alumina feedstock A was modified into feedstock B with additions of an alumina powder with 99.99% purity and an average particle size of  $\sim 0.5$   $\mu\text{m}$ , which reduced the average size of the alumina blend to 1.1  $\mu\text{m}$ . Reduction of the particle size and increasing the sintering temperature of samples printed with alumina feedstock B from 1625 °C to 1650 °C resulted in sintered densities of 97–98% theoretical density with virtually no open porosity. This small improvement in density and a reduced open porosity should make alumina feedstock B plates essentially impermeable even at low plate thicknesses. If impermeability is not achieved, the cause is most likely due to problems associated with the 3D-printing process and not the feedstock.

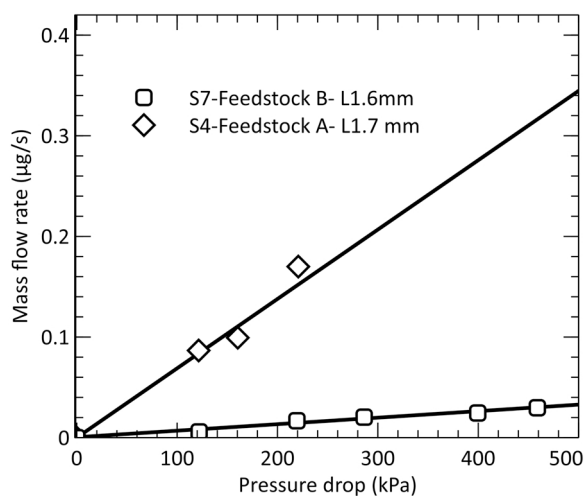


Fig. 6. Mass flow rate versus pressure drop for a 1.6-mm-thick alumina 3D-printed plate made of feedstock B.

The alumina feedstock B was utilized to 3D-print two new ceramic plates with thicknesses of 1.6 (i.e., sample S7) and 3.2 mm (i.e., sample S8). Fig. 6 compares the mass flow rate of the gas leaked through two 3D-printed plates made of alumina feedstock A (i.e., sample S4) and B (i.e., sample S7) versus pressure potentials across the plates. As evident, the alumina plate made of feedstock B demonstrates a significantly lower leaked mass flow rate compared with that of the alumina plate 3D-printed with feedstock A. The slopes of the curves for the alumina plates made of feedstock A and B are  $8 \times 10^{-11}$  and  $10^{-13}$  kg/Pa-s, respectively. This indicates that the permeability of the alumina plate 3D-printed with feedstock B is  $2.35 \times 10^{-6}$  millidarcy, which is almost two orders of magnitude lower than a similar thickness plate fabricated with alumina feedstock A. It should be noted that sample S8, made of alumina feedstock B and a thickness of 3.2 mm, showed no leakage and thus is impermeable. In contrast, 3D-printed plates made of alumina feedstock A showed impermeability at a thickness of 5 mm.

#### 4.2. Ceramic 3D-printed curved tubes

The promising results achieved with the ceramic 3D-printed plates inspired the fabrication of more functional 3D-printed parts. To this end, alumina tubes were 3D-printed to mimic tubes and curved manifolds of a typical heat exchanger design. As shown in Fig. 7, three tubes with different wall thicknesses were examined to study the leakage rate of ceramic 3D-printed tubes. The wall thicknesses of tubes 1, 2, and 3 were 1.92, 1.9, and 0.9 mm, respectively. The intrinsic leakage rate of the test setup was established against a metal tube. Leakage test results demonstrated that the alumina 3D-printed tubes 1 and 2 are impermeable to a gas flow. In contrast, the alumina 3D-printed tube 3 with a

lower wall thickness of 0.9 mm was permeable to the gas flow. Fig. 8 shows the mass flow rate of the gas leaked through the 3D-printed tube 3 at different pressure potentials between inside and outside of the tube. As shown, the leaked gas flow rate linearly increases with the pressure potential as predicted by the Darcy's formula. The slope of the fitted curve is  $5.6 \times 10^{-17}$  kg/Pa-s resulting in a permeability value of  $9.6 \times 10^{-7}$  millidarcy.

A comprehensive study is required to understand the temperature-leakage dependency of the alumina 3D-printed samples at high temperatures and pressures. Generally, an increase in the leakage rate is expected at high temperatures due to thermal expansion of micro-cracks if present. A series of preliminary high-temperature high-pressure tests were conducted to evaluate the leakage rate of the alumina 3D-printed tube with a wall thickness of 1.9 mm that was proved to be impermeable at room temperature. The alumina 3D-printed tube did not show any measurable leakage rate under the combined high temperatures and pressures of 300 °C / 0.7 MPa, 350 °C / 1 MPa, and 400 °C / 1.4 MPa. In the future, additional testing will be conducted at higher temperatures and pressures to thoroughly examine the leakage rate of the alumina 3D-printed modules at various wall thicknesses.

#### 4.3. Ceramic 3D-printed cell-scale HXs with horizontal and vertical separating walls

Next, alumina 3D-printed cell-scale heat exchangers with an overall size of 5 cm × 5 cm × 1 cm were fabricated to investigate the leakage rate of ceramic 3D-printed parts in a more realistic HX configuration. The HX was 3D-printed with alumina feedstock A, resulting in a 96% theoretical density (cf. Fig. 9a). A pressure difference of 344.7 kPa

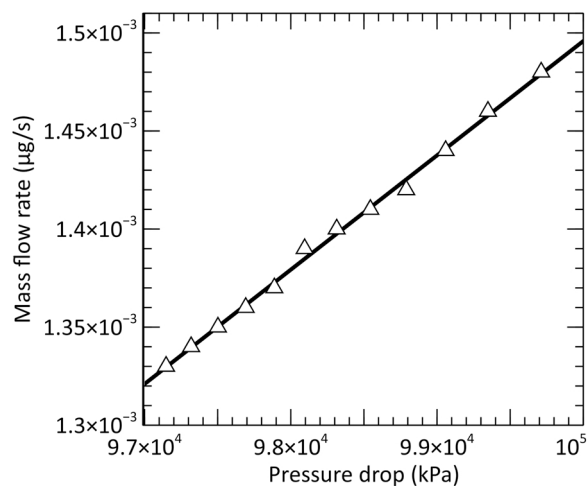


Fig. 8. Mass flow rate versus pressure drop for a 0.9-mm-thick alumina 3D-printed tube.

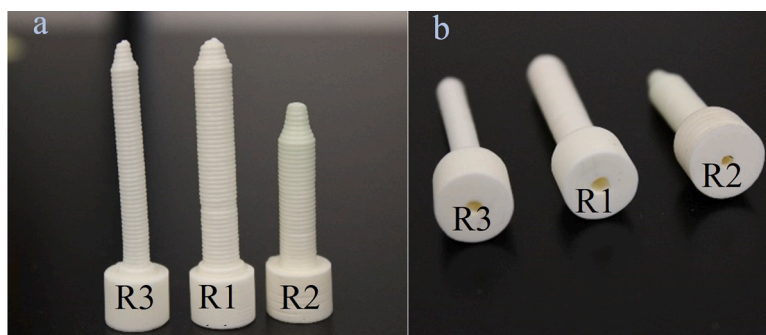
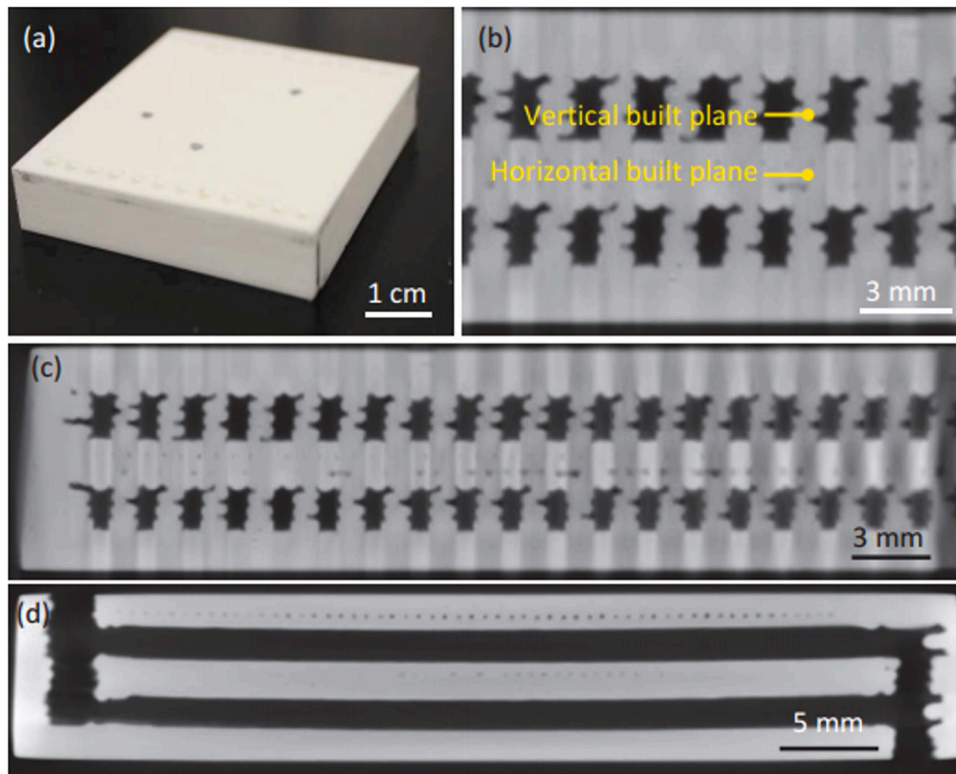
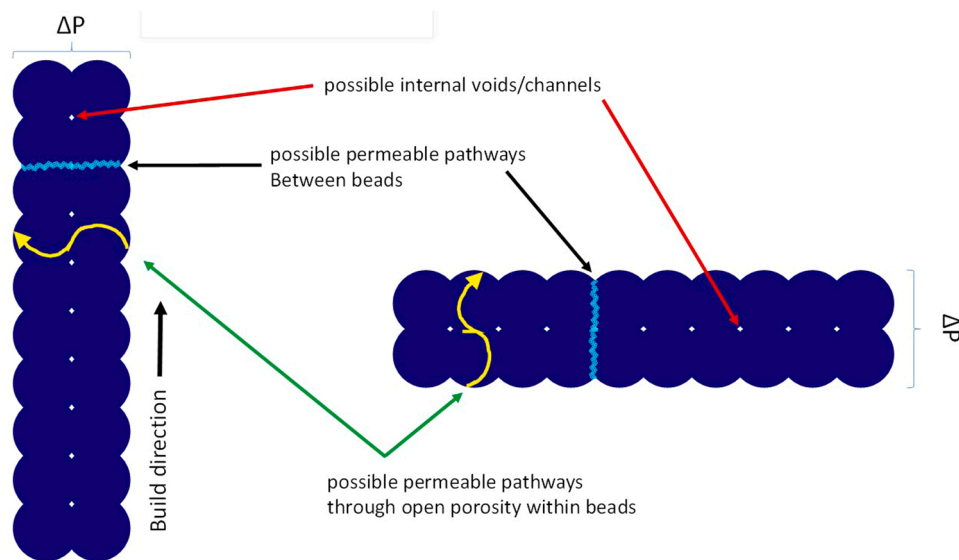


Fig. 7. Alumina 3D-printed tubes: (a) front view, and (b) cross-sectional view.



**Fig. 9.** Alumina 3D-printed HX made of alumina composition A: (a) an overall HX image, (b) CT scan of a zoomed cross-sectional view, (c) CT scan of an x-dir. cross-sectional view, and (d) CT scan of a y-dir. cross-sectional view.



**Fig. 10.** Possible permeable pathways through an extrusion-based 3D-printed structure.

(50 psi) between hot and cold channels was established to evaluate quality of the 3D-printed heat exchanger. The alumina 3D-printed heat exchanger, however, demonstrated an unacceptable internal leakage rate between hot and cold channels. Hence, the alumina 3D-printed HX was scanned with X-ray computed tomography (CT) in Zeiss equipment to better understand the shape of internal features upon ceramic 3D printing and sintering. Fig. 9b-d show the CT scans of the 3D-printed HX made of alumina composition A. The CT scan images were able to provide significant manufacturing insights, which were not possible with conventional procedures unless destructive approaches were adopted. It

is evident that the printing direction (i.e., horizontal vs. vertical build plane) has a distinct effect on the quality of the alumina 3D-printed separating walls. As shown, vertical walls demonstrate a scallop shape with a non-uniform layer thickness (Fig. 9b and c). Particularly, the thickness of a vertically 3D-printed plate locally becomes very thin with a possibility of a high local leakage rate. In contrast, horizontally 3D-printed plates exhibit a higher quality with a uniform layer thickness, as evident in Fig. 9d.

The schematic in Fig. 10 depicts possible permeable pathways through an extrusion-based 3D-printed structure. As shown, beads of an

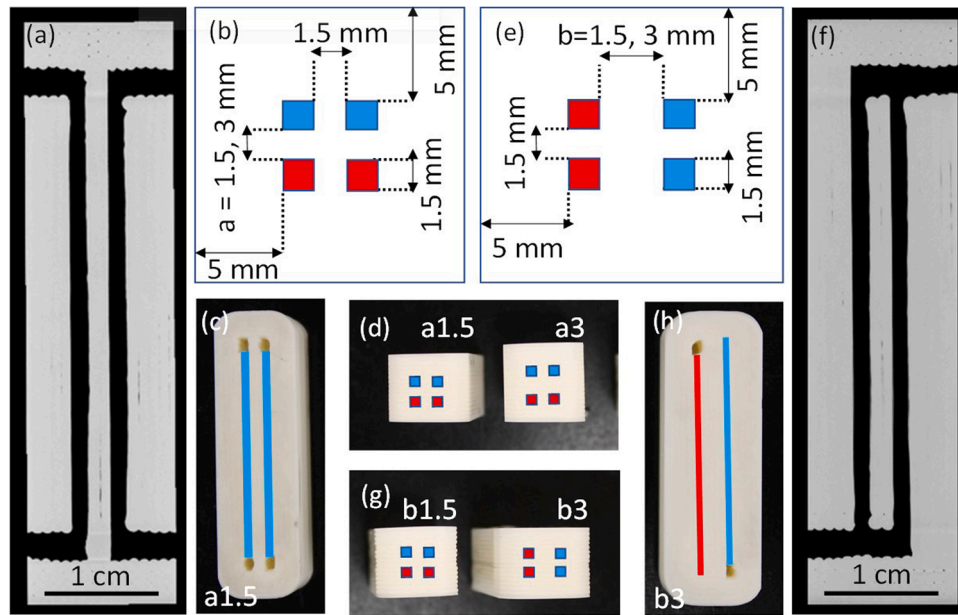


**Fig. 11.** (a) A CT scan cross-sectional view of Type a HX, (b) a schematic cross-sectional view of Type a HX, (c) a front view image of Type a HX, (d) a cross-sectional view image of Type a HX, (e) a schematic cross-sectional view of Type b HX, (f) a CT scan cross-sectional view of Type b HX, (g) a cross-sectional view image of Type b HX, and (h) a front view image of Type b HX. The blue and red colors represent the cold and hot flow streams.

**Table 1**

Internal leakage test results of the four alumina cell-scale 3D-printed HXs with horizontal and vertical separating walls. All four 3D-printed HX configurations showed zero external leakage.

Configuration number	Built print direction	Thickness of separating wall	Test duration	Average internal leakage rate [kg/s]	Internal permeability
a1.5	Horizontal	1.5 mm	12 hrs	0	Impermeable
a3	Horizontal	3 mm	12 hrs	0	Impermeable
b1.5	Vertical	1.5 mm	12 hrs	$6.1 \times 10^{-16}$	Permeable $\kappa = 7.2 \times 10^{-5}$ md
b3	Vertical	3 mm	12 hrs	0	Impermeable

extruded slurry are deposited next to and on top of each other. Therefore, the permeability of a solid 3D-printed part depends on (i) interconnected porosity within the material due to possible air pockets present in the feedstock slurry, (ii) how well the extruded beads join together during the printing process, and (iii) fusion quality of ceramic particles during the sintering process. Particularly, the second factor depends on the print orientation; horizontal versus vertical printing

direction. The microstructure between layers that form a vertical barrier (cf., the left schematic in Fig. 10) can be different than the microstructure between beads that are deposited next to each other within a single layer (cf., the right schematic in Fig. 10). Also, beads that do not completely flow together can leave macroscopic channel-shaped voids parallel to the build direction. Therefore, permeability data collected for flat plates are not adequate to predict the complexities of real heat exchanger designs.

Cell-scale alumina HXs with horizontal (i.e., Type a) and vertical (i.e., Type b) separating walls between the hot and cold sides were 3D-printed to study the effect of 3D-printing direction on the permeability of 3D-printed parts. Fig. 11 shows schematics and actual images of the cell-scale 3D-printed HX modules for permeability tests. For simplicity, heat exchangers were designed with only four channels (i.e., two hot and two cold channels). In addition, two different thicknesses of 1.5 and 3 mm were considered for each HX type making a total of four different configurations. In type a, cold and hot flow streams were separated from each other with a horizontal separating as shown in Fig. 11a-d. Two HX designs with horizontal wall thicknesses of 1.5 (Type a1.5) and 3 mm (Type a3) were fabricated. In type b, the plates separating cold and hot flow streams were 3D-printed in a vertical build direction (cf. Fig. 11e-h). Similarly, two HX designs with vertical wall thicknesses of 1.5 (Type b1.5) and 3 mm (Type b3) were considered. None of the four channels in types a and b are interconnected.

The four alumina 3D-printed HXs were extensively tested for the leakage rate. The test results demonstrated that the permeability of ceramic 3D-printed modules depends on the printing direction. Both internal (i.e., between cold and hot flow channels) and external (between cold/hot channels and outside environment) leakage tests were

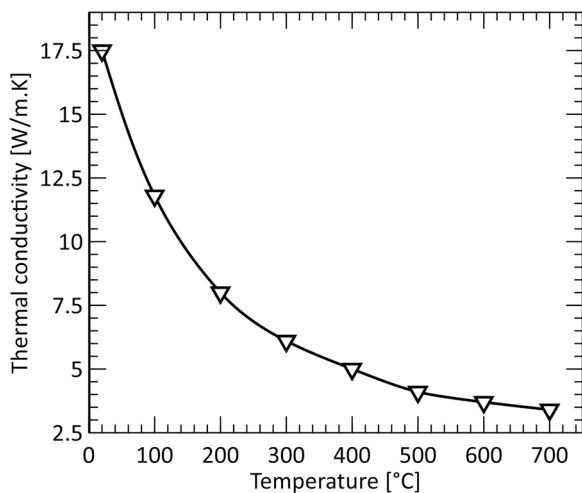


**Fig. 12.** Thermal conductivity of an alumina 3D-printed coupon densified to 96% of theoretical density as a function of temperature.

examined. All four cell-scale HX modules showed zero external leakage. Table 1 provides internal leakage test results of four cell-scale alumina 3D-printed HX designs with horizontal and vertical separating walls. When the thickness of the wall separating the cold and hot sides is 3 mm (i.e., Type a3 and b3 HXs), the cell-scale alumina 3D-printed HXs demonstrated a zero-permeability independent of the 3D-printing build direction. It is evident that the 3D-printing build direction affects internal permeability values of the cell-scale HXs with 1.5-mm-thick horizontal (i.e., Type a1.5) and vertical (i.e., Type b1.5) plates. As shown, type a1.5 HX with a horizontal separating wall of 1.5 mm is impermeable. However, type b1.5 HX with a vertical separating wall of 1.5 mm showed an internal permeability of  $7.2 \times 10^{-5}$  millidarcy. This confirms that a horizontally built plate has a higher 3D-printing quality consistent with the X-ray CT scan imaging.

The thermal conductivity of an alumina 3D-printed coupon was measured at high temperatures to have a better insight into the design of functional ceramic heat exchanger systems. Thermal conductivity is an important material characteristic affecting the overall thermo-hydraulic performance of a ceramic 3D-printed heat exchanger. Thermal conductivity is particularly important for ceramic 3D-printed heat exchangers as their thermal conductivities are significantly lower than typical metals due to the absence of free electrons. Fig. 12 shows variations of thermal conductivity of an alumina 3D-printed coupon as a function of temperature. The alumina 3D-printed coupon was sintered and densified to 96% of theoretical density (i.e., a density of 3975 kg/m<sup>3</sup>). As shown, the thermal conductivity is inversely related to the sample temperature due to anharmonic phonon scattering (i.e., phonon-phonon interactions). At room temperature, the thermal conductivity of the alumina 3D-printed sample is 18 W/m-K. The thermal conductivity of the alumina 3D-printed sample decreases from 11.8 to 3.4 W/m-K when the sample temperature increases from 100° to 700°C. In the future, alumina 3D-printed heat exchangers employing complex heat transfer topologies will be developed, considering the fundamental properties of ceramic 3D-printed modules studied in this work.

## 5. Conclusion

In this study, the argon gas leakage rate of alumina 3D-printed modules consisting of flat plates, curved tubes, and cell-scale plate-and-frame HXs was systematically examined. Effects of several parameters, including feedstock slurry, 3D-printing direction, and post-processing conditions on leakage rate of alumina 3D-printed parts, were examined to identify the minimum thickness required for impermeability. Two alumina feedstock compositions of A (i.e., a 99.8% purity alumina powder with an average particle size of 1.9 μm) and B (i.e., a 99.9% high-purity alumina powder with an average particle size of ~0.5 μm) resulting sintered alumina densities of 96% and 98% of theoretical density were examined.

A noticeable change in permeability of 3D-printed flat plates made of alumina feedstock A and B were identified. While a minimum thickness of 5 mm was required to achieve impermeability with feedstock slurry A, impermeability was accomplished at a plate thickness of 3.2 mm with feedstock slurry B. A 0.75-mm-thick alumina 3D-printed plate made of feedstock A showed a permeability of  $6 \times 10^{-4}$  millidarcy. The gas leakage rate of alumina 3D-printed tubes and cell-scale HXs were examined with alumina feedstock B. While an alumina 3D-printed tube with a thickness of 1.9 mm was impermeable to a gas flow, a 0.9-mm-thick tube showed a permeability of  $9.6 \times 10^{-7}$  millidarcy. Additionally, alumina cell-scale HXs employing horizontal 3D-printed walls separating cold and hot streams yielded impermeability at 1.5 and 3 mm wall thicknesses. An alumina cell-scale HX utilizing 1.5-mm-thick vertical 3D-printed separating walls demonstrated a gas permeability of  $7.2 \times 10^{-5}$  millidarcy. Experiments conducted here confirmed the promise of ceramic 3D-printed modules to accelerate the development of next-generation high-temperature high-pressure sCO<sub>2</sub> power cycles.

## CRedit authorship contribution statement

**Rasoul Bayaniahangar:** Investigation, Data curation, Visualization, Writing – original draft preparation. **Ikechukwu Okoh:** Investigation, Writing – original draft preparation. **Kashif Nawaz:** Supervision, Writing – original draft preparation. **Joseph Cesarano:** Supervision, Writing – original draft preparation. **Sajjad Bigham:** Conceptualization, Supervision, Methodology, Writing – original draft preparation, Writing – review & editing.

## Declaration of Competing Interest

The authors declare that they have no known competing financial interests or personal relationships that could have appeared to influence the work reported in this paper.

## Acknowledgments

This study was sponsored by the Advanced Research Projects Agency-Energy (ARPA-E), U.S. Department of Energy, under Award Number DE-AR0001126. The authors would like to acknowledge Prof. Michael Ohadi, Program Manager, Prof. Zak Fang, Program Manager, Dr. Pankaj Trivedi, Tech-SETA, and Dr. Vivien Lecoustre, Tech-SETA of ARPA-E's HITEMMP (High Intensity Thermal Exchange through Materials and Manufacturing Processes) program. The authors also acknowledge Oak Ridge National Laboratory staff for X-ray CT scanning.

## References

- [1] M. Mehos, C. Turchi, J. Vidal, M. Wagner, Z. Ma, C. Ho, W. Kolb, C. Andraka, A. Kruiženga, Concentrating Solar Power Gen3 Demonstration Roadmap, National Renewable Energy Lab.(NREL), Golden, CO (United States), 2017.
- [2] C.S. Turchi, Z. Ma, T.W. Neises, M.J. Wagner, Thermodynamic study of advanced supercritical carbon dioxide power cycles for concentrating solar power systems, *J. Sol. Energy Eng.* 135 (2013).
- [3] M. Ohadi, X. Zhang, H. Keramati, M. Arie, F. Singer, R. Tiwari, A. Shooshtari, Recent developments in high temperature heat exchangers: A review, *Front. Heat. Mass Transf.* 11 (2018).
- [4] Q. Li, G. Flamant, X. Yuan, P. Neveu, L. Luo, Compact heat exchangers: A review and future applications for a new generation of high temperature solar receivers, *Renew. Sustain. Energy Rev.* 15 (2011) 4855–4875.
- [5] M.A. Wilson, K. Recknagle, K. Brooks, Design and development of a low-cost, high temperature silicon carbide micro-channel recuperator, *Turbo Expo. Power Land, Sea, Air* (2005) 1029–1034.
- [6] C. Lewinsohn, High-efficiency, ceramic microchannel heat exchangers, *Am. Ceram. Soc. Bull.* 94 (2015).
- [7] B. Sunden, High temperature heat exchangers (HTHE), *Enhanc. Compact Ultra-Compact Heat. Exch.* 29 (2005) 226–238.
- [8] D. Chen, S. Heyer, S. Ibbotson, K. Salonitis, J.G. Steingrímsson, S. Thiede, Direct digital manufacturing: definition, evolution, and sustainability implications, *J. Clean. Prod.* 107 (2015) 615–625.
- [9] S. Ford, M. Despeisse, Additive manufacturing and sustainability: an exploratory study of the advantages and challenges, *J. Clean. Prod.* 137 (2016) 1573–1587.
- [10] M. Mani, K.W. Lyons, S.K. Gupta, Sustainability characterization for additive manufacturing, *J. Res. Natl. Inst. Stand. Technol.* 119 (2014) 419.
- [11] H. Masuda, Y. Ohta, M. Kitayama, Additive Manufacturing of SiC Ceramics with Complicated Shapes Using the FDM Type 3D-Printer, *J. Mater. Sci. Chem. Eng.* 7 (2019) 1.
- [12] M. Innocentini, V.R. Salvini, V.C. Pandolfelli, J.R. Coury, Permeability of ceramic foams, *Am. Ceram. Soc. Bull.* 78 (1999) 78–84.
- [13] M. Lipowiecki, M. Rývolová, Á. Tóttösi, N. Kolmer, S. Naher, S.A. Brennan, M. Vázquez, D. Brabazon, Permeability of rapid prototyped artificial bone scaffold structures, *J. Biomed. Mater. Res. Part A.* 102 (2014) 4127–4135.
- [14] A. Dey, N. Kayal, O. Chakrabarti, R.F. Caldato, C.M. André, M.D.M. Innocentini, Permeability and nanoparticle filtration assessment of cordierite-bonded porous SiC ceramics, *Ind. Eng. Chem. Res.* 52 (2013) 18362–18372.
- [15] A. Gómez-Martín, M.P. Orihuela, J.A. Becerra, J. Martínez-Fernández, J. Ramírez-Rico, Permeability and mechanical integrity of porous biomorphic SiC ceramics for application as hot-gas filters, *Mater. Des.* 107 (2016) 450–460.
- [16] L. Biasetto, P. Colombo, M.D.M. Innocentini, S. Mullens, Gas permeability of microcellular ceramic foams, *Ind. Eng. Chem. Res.* 46 (2007) 3366–3372.
- [17] E.A. Moreira, M.D.M. Innocentini, J.R. Coury, Permeability of ceramic foams to compressible and incompressible flow, *J. Eur. Ceram. Soc.* 24 (2004) 3209–3218.
- [18] C. Schmitt, D.W. Agar, F. Platte, S. Buijssen, B. Pawlowski, M. Duisberg, Ceramic plate heat exchanger for heterogeneous gas-phase reactions, *Chem. Eng. Technol.* 28 (2005), <https://doi.org/10.1002/ceat.200407119>.

- [19] G. Amirthan, M. Balasubramanian, Helium gas permeability of SiC tubes produced using cotton fabric, *Ceram. Int.* 41 (2015), <https://doi.org/10.1016/j.ceramint.2014.11.020>.
- [20] P.F. Peterson, H. Zhao, F. Niu, W. Huang, J. Schmidt, J. Schulte-Fischedick, Development of C-SiC ceramic compact plate heat exchangers for high temperature heat transfer applications, in: *AIChE Annu. Meet. Conf. Proc.*, 2006.
- [21] J. Schmidt, M. Scheffele, M. Crippa, P.F. Peterson, E. Urquiza, K. Sridharan, L. C. Olson, M.H. Anderson, T.R. Allen, Y. Chen, Design, fabrication, and testing of ceramic plate-type heat exchangers with integrated flow channel design, *Int. J. Appl. Ceram. Technol.* 8 (2011), <https://doi.org/10.1111/j.1744-7402.2010.02573.x>.
- [22] C. Bouquet, A. Luc-Bouhali, B. Hauber, J. Thebault, Validation of a leak-free C/SiC heat exchanger technology, in: *12th AIAA Int. Sp. Planes Hypersonic Syst. Technol.*, 2003. <https://doi.org/10.2514/6.2003-6918>.
- [23] D. Hayasaka, H. Kishimoto, A. Kohyama, Helium permeability of high-performance SiC/SiC tube, *J. Nucl. Sci. Technol.* 53 (2016), <https://doi.org/10.1080/00223131.2016.1184107>.